Research Article

Jonathan Rincon Saucedo, Antonio Paz, F. V. Flores-Baez, and Jose Ruben Morones Ibarra*

Influence of the regularization scheme in the QCD phase diagram in the PNJL model

Abstract: In the context of the SU(2) quark flavor version of the Nambu–Jona-Lasinio model extended by the Polyakov loop, the effect of the regularization scheme on the quantum chromodynamics phase structure at finite volume was studied. The way in which the phase diagram changes with the type of Polyakov loop potential considered in this study was also investigated. In this study, a polynomial and a logarithmic potential were used. On the other hand, a regularization scheme that satisfies the thermodynamics properties such as the Stefan–Boltzmann limit was chosen.

1 Introduction

The study of the quantum chromodynamics (QCD) phase structure is important in several fields of physics such as cosmology, astrophysics, and particle physics [1,2]. Two kinds of phase diagrams can be studied using the Polyakov–Nambu–Jona-Lasinio (PNJL) model: one is the chiral phase diagram, which is associated with the chiral symmetry restoration in the limit of zero quark masses, and other one is the phase transition from the confined (hadronic phase) to the deconfined phase, which corresponds to the Quark–gluon plasma (QGP) [3–6]. Both phenomena, the chiral phase transition and the confined–deconfined transition, are conceptually different; however, the aim of this study was to investigate whether there is a

relationship between the transition temperature among these processes. In an independent model such as lattice QCD simulation, some authors have found that chiral transition and color deconfinement occur almost at the same temperature [7,8]. The very close crossover lines among both processes suggest that it can be a common dynamical mechanism that relates both transitions. In addition, some authors claimed that within the region that divides these two phases, there is a "critical end point" (CEP), which would indicate a change in the nature of the transition, from a crossover to a first-order phase transition [9–14]. The study of the phase diagram, the location of the CEP, and the properties of the QGP are the main objectives of large experiments carried out by heavy ion colliders [15–17]. To study these type of transitions for matter subjected to extreme temperatures and densities, there are several alternative models. In this study, the PNJL model that allows us to study both phenomena, the chiral transition and the confinement–deconfinement process, by adding an effective potential was used. In order to take into account the effects of finite volumes in the model, the multiple reflection expansion (MRE) approximation by modifying the density of states of the thermodynamic potential was used.

The way in which the QCD phase diagram changes as a function of several parameters and variables, such as temperature, chemical potential, the size of the finite volume, and its geometry was investigated. The effect of the cutoff scheme was included, and the effect of the different Polyakov potential in the phases of QCD was also explored.

2 PNJL model

In the non-perturbative regime of the QCD, there are several alternative effective theories to study the behavior of a system of strongly interacting matter. The main aim of this study was to concentrate on the PNJL model. The main advantage of this model is the inclusion of a "Polyakov loop" acting as an order parameter for gauge theories at non-zero temperatures, which is useful to identify the quark confinement [18–20].

* **Corresponding author: Jose Ruben Morones Ibarra,** Facultad de Ciencias Físico Matemáticas, Universidad Autónoma de Nuevo León, Avenida Universidad S/N, Ciudad Universitaria, San Nicolás de los Garza, N.L. CP. 66455, México, e-mail: rubenmorones@yahoo.com.mx
Jonathan Rincon Saucedo, Antonio Paz, F. V. Flores-Baez: Facultad de Ciencias Físico Matemáticas, Universidad Autónoma de Nuevo León, Avenida Universidad S/N, Ciudad Universitaria, San Nicolás de los Garza, N.L. CP. 66455, México

The Lagrangian for the two-flavor quark version of the PNJL model for three colors is given by [21,22]:

$$\mathscr{L}_{\text{PNJL}} = \bar{q}[i\gamma^\mu D_\mu - m_o + \gamma_o\mu]q$$
$$+ \frac{G}{2}[(\bar{q}q)^2 + (\bar{q}i\gamma_5\tau q)^2] - \mathcal{U}(\varphi, \varphi^*; T), \quad (1)$$

where $m_o = (m_u, m_d)$ represents the current quark masses, and assuming the isospin symmetry, we have $m_u = m_d = m_o$. In the PNJL model in order to incorporate the external gluonic field A_μ (produced by a very heavy quark, which means that it has no dynamics properties), the covariant derivative $D_\mu = \partial_\mu - iA_\mu$ was introduced.

The thermodynamic potential per unit volume is calculated from the partition function Z through the expression $\Omega(T, \mu) = -T \ln Z/V$, which describes the contribution of the color states to the system. Applying the mean field approximation, which is a Taylor expansion around the condensate $\langle\bar{q}q\rangle$, we obtain

$$M = m_o - 2G\langle\bar{q}q\rangle, \quad (2)$$

where M, the quark constitutive mass, is generated by the interaction between the quarks and the condensate $\langle\bar{q}q\rangle \approx -\sigma/2G$. This is the reason to call M the dynamically generated quark mass [23,24].

The thermodynamic potential of the PNJL model in the frame of SU(2) flavor is given by [22]:

$$\Omega_{\text{PNJL}} = \mathcal{U}(\varphi, \varphi^*; T) + \frac{(M - m_o)^2}{4G} - 2N_f N_c \int \frac{d^3\boldsymbol{p}}{(2\pi)^3}$$
$$\times \{E_{\boldsymbol{p}} + T[\ln(1 + e^{-\beta(E_{\boldsymbol{p}}-\mu)}e^{-igA_4\beta}) + \ln(1 + e^{-\beta(E_{\boldsymbol{p}}+\mu)}e^{igA_4\beta})]\}, \quad (3)$$

where the quasi-quark energy is $E_{\boldsymbol{p}} = \sqrt{\boldsymbol{p}^2 + M^2}$, $N_c = 3$, $N_f = 2$, and igA_4 is the time component of the gluonic field in the Euclidean space.

The Wilson line, a color matrix defined in terms of A_4 with $N_c \times N_c$ dimension, was introduced as follows:

$$L(\boldsymbol{x}) = Pe^{i\int_o^\beta A_4 d\tau} = e^{i\beta A_4}. \quad (4)$$

To simplify the expressions, the coupling constant g was substituted into the definition of A_4 in Eq. (4). The importance of $L(x)$ lies in the fact that the gluonic contribution is described by the potential $\mathcal{U}(\Phi, \Phi^*)$, whose dynamics depends on a complex field called the Polyakov loop [25–27]:

$$\Phi(\boldsymbol{x}) = \frac{1}{N_c}\text{Tr}[L(\boldsymbol{x})],$$
$$\Phi^*(\boldsymbol{x}) = \frac{1}{N_c}\text{Tr}[L^\dagger(\boldsymbol{x})]. \quad (5)$$

If we replace these terms in our thermodynamic potential, we obtain our final Ω:

$$\Omega_{\text{PNJL}} = \mathcal{U}(\varphi, \varphi^*; T) + \frac{(M - m_o)^2}{4G} - 2N_f N_c \int \frac{d^3\boldsymbol{p}}{(2\pi)^3}$$
$$\times \{E_{\boldsymbol{p}} + T[\ln(1 + L^\dagger e^{-\beta(E_{\boldsymbol{p}}-\mu)}) + \ln(1 + e^{-\beta(E_{\boldsymbol{p}}+\mu)}L)]\}. \quad (6)$$

In this study, two different Polyakov loop potentials $\mathcal{U}$ (one of them is a polynomial and the other one is a logarithmic function) were used [22,28,29]. For the polynomial potential, we use the following expression:

$$\mathcal{U} = T^4\left[-\frac{b_2(T)}{2}\Phi\Phi^* - \frac{b_3}{6}(\Phi^3 + \Phi^{*3}) + \frac{b_4}{4}(\Phi\Phi^*)^2\right], \quad (7)$$

where

$$b_2 = a_0 + a_1\left(\frac{T_0}{T}\right) + a_2\left(\frac{T_0}{T}\right)^2 + a_3\left(\frac{T_0}{T}\right)^3, \quad (8)$$

with parameters $a_0 = 6.76, a_1 = -1.95, a_2 = 2.625, a_3 = -7.44$, $T_0 = 270$ MeV, $b_3 = 0.75$, and $b_4 = 7.5$.

The logarithmic potential allows us to limit the Polyakov loop to be less than 1, and this potential is given by:

$$\mathcal{U} = T^4\left[-\frac{a(T)}{2}\Phi\Phi^* + b(T)\ln[1 - 6\Phi\Phi^* + 4(\Phi^3 + \Phi^{*3}) - 3(\Phi\Phi^*)^2]\right], \quad (9)$$

with

$$a(T) = a_0 + a_1\left(\frac{T_0}{T}\right) + a_2\left(\frac{T_0}{T}\right)^2, \quad (10)$$

$$b(T) = b_3\left(\frac{T_0}{T}\right)^3. \quad (11)$$

The values for the parameters are $a_0 = 3.51$, $a_1 = -2.47$, $a_2 = 15.2$, $b_3 = -1.75$, and $T_0 = 270$ MeV [30].

Once the potential $\mathcal{U}$ is chosen, we can minimize the thermodynamic potential using the condition $\partial\Omega/\partial\sigma = 0$, in order to obtain the thermodynamic equilibrium. This leads to the gap equation from which we can calculate the constitutive quark masses M as follows:

$$M - m_o - 4GN_cN_f\int dp \frac{p^2}{2\pi^2}\frac{M}{E_{\boldsymbol{p}}}[1 - g^{(+)} - g^{(-)}] = 0, \quad (12)$$

where the functions $g^{(+)}$ and $g^{(-)}$ are determined by:

$$g^{(\pm)} = \frac{\Phi e^{-\beta(E_p\pm\mu)} + 2\Phi^* e^{-2\beta(E_p\pm\mu)} + e^{-3\beta(E_p\pm\mu)}}{1 + 3\Phi e^{-\beta(E_p\pm\mu)} + 3\Phi^* e^{-2\beta(E_p\pm\mu)} + e^{-3\beta(E_p\pm\mu)}}. \quad (13)$$

The minimization of the thermodynamic potential must be performed for each mean field, which results in a self-consistent system of equations to be solved numerically:

$$\frac{\partial \Omega}{\partial \sigma} = 0, \frac{\partial \Omega}{\partial \Phi} = 0, \quad \text{and} \quad \frac{\partial \Omega}{\partial \Phi^*} = 0. \tag{14}$$

The solutions for this system are the chiral $\langle \sigma \rangle$, Polyakov loop $\langle \Phi \rangle$ and $\langle \Phi^* \rangle$ expectation values.

In summary, the PNJL model is obtained by adding a gluonic potential in the Lagrangian of the Nambu–Jona-Lasinio (NJL) model. This gluonic potential is written in terms of the Polyakov loop. The Polyakov loop is an order parameter that helps to identify the confinement–deconfinement transition. The confinement condition corresponds to $\Phi(x) = 0$, and any value, $\Phi(x) \neq 0$, implies a deconfined phase.

3 Regularization schemes

The PNJL model is a non-renormalizable effective model whose thermodynamic potential is integrated over the entire momentum space. This represents a problem since it leaves us with divergent integrals [31,32].

Let us take, for example, the gap in Eq. (12). The first integral is clearly divergent since it has to be evaluated in the entire space of momenta. Therefore, it is necessary to use a regularization scheme to bound the integral:

$$\int \mathrm{d}p \frac{p^2}{2\pi^2} \cdot \frac{M}{E_p} = \int \mathrm{d}p \frac{p^2}{2\pi^2} \frac{M}{\sqrt{p^2 + M^2}}. \tag{15}$$

Also, we have to use some criteria to manage the other integrals, which means to use a regularization scheme that makes the mathematical treatment physically consistent.

3.1 Three-dimensional ultraviolet UV cutoff

One regularization method to eliminate these UV divergences is to impose a three-dimensional cutoff in the divergent integral. This method can preserve the structure of the gap equations, but the Lorentz invariance is broken. However, this is not a drawback since in the finite temperature and chemical potential framework, the Lorentz invariance is not preserved.

To apply the three-dimensional UV cutoff, we impose an upper limit Λ to the integral. If the integrand possesses spherical symmetry, the integral will be modified as follows [33,34]:

$$\int \frac{\mathrm{d}^3 \boldsymbol{p}}{(2\pi)^3} \to \int_0^\Lambda \frac{\mathrm{d}p\, p^2}{2\pi^2}. \tag{16}$$

It is important to remark that we have chosen this regularization method in our calculations; however, we should mention that there are many other methods, each one with its advantages and disadvantages, such as: Pauli–Villars regularization and proper-time regularization [35].

3.2 Cutoff schemes

Once we have chosen the three-dimensional UV cutoff as our regularization method, our main interest is to investigate how this cutoff affects the integrals and our calculations. In the SU(2) framework of the PNJL model, the thermodynamic potential before the application of any cutoff is given by [22,26,36]:

$$\Omega_{\mathrm{PNJL}} = \mathcal{U}(\varphi, \varphi^*; T) + \frac{\sigma^2}{4G} - 2N_f N_c \int_0^\infty$$
$$\times \frac{\mathrm{d}^3 \boldsymbol{p}}{(2\pi)^3} E_{\boldsymbol{p}} - 2N_f N_c T \int_0^\infty \frac{\mathrm{d}^3 \boldsymbol{p}}{(2\pi)^3} \tag{17}$$
$$\times [\ln(1 + L^\dagger e^{-\beta(E_{\boldsymbol{p}} - \mu)}) + \ln(1 + e^{-\beta(E_{\boldsymbol{p}} + \mu)} L)].$$

If we impose our regularization scheme to all integrals in Ω_{PNJL}, integrating up to a common cutoff, we obtain a new potential that is different from the obtained when we do not apply the cutoff to the integrals that does need it, such as the integrals that depend on the temperature. This scheme of regularization is usually called "maximal cutoff." The thermodynamic potential takes the form:

$$\Omega_{\mathrm{PNJL}}^{\max} = \mathcal{U}(\varphi, \varphi^*; T) + \frac{\sigma^2}{4G} - 12 \int_0^\Lambda \frac{\mathrm{d}^3 \boldsymbol{p}}{(2\pi)^3} E_{\boldsymbol{p}}$$
$$- 12T \int_0^\Lambda \frac{\mathrm{d}^3 \boldsymbol{p}}{(2\pi)^3} [\ln(1 + L^\dagger e^{-\beta(E_{\boldsymbol{p}} - \mu)}) + \ln(1 \tag{18}$$
$$+ e^{-\beta(E_{\boldsymbol{p}} + \mu)} L)].$$

However, this last equation gives us an incomplete thermodynamic description since it does not satisfy the Stefan–Boltzmann limit [31].

Our first proposal would be to modify the limits of the second integral, Eq. (18), which is already convergent. We call this new scheme "minimal cutoff" [29]:

$$\Omega_{\mathrm{PNJL}}^{\min} = \mathcal{U}(\varphi, \varphi^*; T) + \frac{\sigma^2}{4G} - 12 \int_0^\Lambda \frac{\mathrm{d}^3 \boldsymbol{p}}{(2\pi)^3} E_{\boldsymbol{p}}$$
$$- 12T \int_0^\infty \frac{\mathrm{d}^3 \boldsymbol{p}}{(2\pi)^3} [\ln(1 + L^\dagger e^{-\beta(E_{\boldsymbol{p}} - \mu)}) + \ln(1 \tag{19}$$
$$+ e^{-\beta(E_{\boldsymbol{p}} + \mu)} L)].$$

Although the minimal cutoff potential takes into account the high momentum modes, which are necessary to reproduce the Stefan–Boltzamann limit of the pressure

at very high temperatures, there are some inconsistencies we must deal with. First, we are treating differently two terms of the same equation, *i.e.*, for the divergent integral, we take the Λ limit, and for the convergent integral, we take the upper limit to infinity. Second, by taking the integral to infinity, we are including the interactions of fermions with the condensate, after the UV cutoff.

To avoid these problems, a new form of potential is proposed, where we continue with the UV cutoff in the divergent integral, but the thermal quark energy is modified in $\sigma = 0$ for all momenta $p > \Lambda$ [30]. This procedure eliminates the fermion–condensate interaction for momenta after the cutoff $p > \Lambda$. This regularization scheme is known as "soft cutoff" and will be the basis of this study. Therefore,

$$
\begin{aligned}
\Omega_{\mathrm{PNJL}}^{\mathrm{soft}} = \mathcal{U}(\varphi, \varphi^*; T) + \frac{\sigma^2}{4G} - 12 \int_0^\Lambda \frac{\mathrm{d}^3 \boldsymbol{p}}{(2\pi)^3} E_{\boldsymbol{p}} \\
- 12T \int_0^\Lambda \frac{\mathrm{d}^3 \boldsymbol{p}}{(2\pi)^3} [\ln(1 + L^\dagger e^{-\beta(E_{\boldsymbol{p}} - \mu)}) + \ln(1 \\
+ e^{-\beta(E_{\boldsymbol{p}} + \mu)} L)] \\
- 12T \int_\Lambda^\infty \frac{\mathrm{d}^3 \boldsymbol{p}}{(2\pi)^3} [\ln(1 + L^\dagger e^{-\beta(E_{\boldsymbol{p}|\sigma=0} - \mu)}) + \ln(1 \\
+ e^{-\beta(E_{\boldsymbol{p}|\sigma=0} + \mu)} L)].
\end{aligned}
\tag{20}
$$

By this modification, we take into account that the interaction of fermions at very high momenta is off in the second term, which would be the correct way to represent the thermodynamic potential at very high temperatures.

4 Finite volume

When the volume of a thermodynamic system is finite, the analysis of phase transition requires adjustments due to finite-size effects, which will modify the thermodynamic calculations. To study the problem with finite volume, we need to introduce boundary conditions and also consider the shape of the volume. In this study, we will analyze the cases of spherical and cubic volumes.

The effects of a finite volume are taken into account by using the MRE approximation, which was developed for a two-flavor NJL model to study the size dependence of the thermodynamic potential for a spherical volume for SU(2) [37]. We extend this approximation to the SU(2) flavor of the PNJL model.

In the MRE framework, the density of states is composed of three terms, which correspond to volumetric, surface, and curvature contributions [38,39]:

$$
\rho_{\mathrm{MRE}} = \rho_{\mathrm{vol}} + \rho_{\mathrm{surf}} f_S + \rho_{\mathrm{curv}} f_C,
\tag{21}
$$

where functions f_S and f_C are the factors of the surface and curvature terms of the fermionic density of states, respectively.

Using the previous equation, the integral in the gap equation changed to:

$$
\begin{aligned}
\int \mathrm{d}p \frac{p^2}{2\pi^2} f(T, \mu, \boldsymbol{p}) &\to \int_0^\infty \mathrm{d}p \rho(p) f(T, \mu, p) \\
&\to \int_{\Lambda_{\mathrm{IR}}}^{\Lambda_{\mathrm{UV}}} \mathrm{d}p \rho_{\mathrm{MRE}}(p, \alpha, R) f(T, \mu, p).
\end{aligned}
\tag{22}
$$

For the purposes of MRE, the upper limit of the integral is given by the tri-momentum cutoff Λ_{UV}, while the infrared cutoff Λ_{IR} will be dependent on the boundary conditions.

The MRE approximation was developed to impose the condition of finite volume for spherical droplets, and we also extend its application to approximate the conditions for a cubic box. For a spherical volume, we also define the Dirichlet and Neumann boundary conditions.

4.1 Spherical volume

For the spherical droplet model, the fermionic density of states, $\rho = \frac{p^2}{(2\pi)^2}$, is replaced with an MRE density of states, ρ_{MRE}, which have three terms [37,39,40]:

$$
\rho_{\mathrm{MRE}} = \frac{p^2}{2\pi^2} \left[1 + \frac{6\pi^2}{pR} f_S + \frac{12\pi^2}{(pR)^2} f_C \right],
\tag{23}
$$

where R is the radius of the sphere and f_S and f_C are given by:

$$
f_S\left(\frac{p}{\alpha}\right) = -\frac{1}{8\pi} \left[1 - \frac{2}{\pi} \arctan \frac{p}{\alpha} \right],
\tag{24}
$$

$$
f_C\left(\frac{p}{\alpha}\right) = \frac{1}{12\pi^2} \left[1 - \frac{3p}{2\alpha} \left(\frac{\pi}{2} - \arctan \frac{p}{\alpha} \right) \right].
\tag{25}
$$

These two functions are affected by boundary conditions, which impose values on the α parameter. The Dirichlet boundary condition is obtained by imposing $\alpha \to \infty$, which means that

$$
\lim_{\alpha \to \infty} f_S\left(\frac{p}{\alpha}\right) = -\frac{1}{8\pi},
\tag{26}
$$

$$
\lim_{\alpha \to \infty} f_C\left(\frac{p}{\alpha}\right) = \frac{1}{12\pi^2},
\tag{27}
$$

and consequently, the density of states for the Dirichlet condition is

$$\rho_{\mathrm{MRE}} = \frac{p^2}{2\pi^2}\left[1 - \frac{3\pi}{4pR} + \frac{1}{(pR)^2}\right]. \tag{28}$$

In the case of the Neumann conditions, the value imposed is $\alpha \to 0$, and then,

$$\lim_{\alpha \to 0} f_S\left(\frac{p}{\alpha}\right) = 0, \tag{29}$$

$$\lim_{\alpha \to 0} f_C\left(\frac{p}{\alpha}\right) = -\frac{1}{24\pi^2}, \tag{30}$$

so that the density of states for the Neumann conditions is

$$\rho_{\mathrm{MRE}} = \frac{p^2}{2\pi^2}\left[1 - \frac{1}{2(pR)^2}\right]. \tag{31}$$
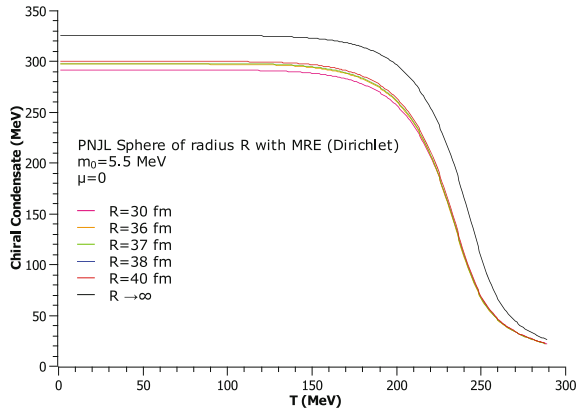
Since the MRE density of states in Eq. (23) has a quadratic term, it is required to impose a lower limit cutoff to avoid a range of negative momentum values, which are not physically acceptable. The Λ_{IR} cutoff is different for each boundary condition obtained for Eqs (28) and (31). The values are $\Lambda_{\mathrm{IR}} = 1.8/R$ for the Dirichlet boundary
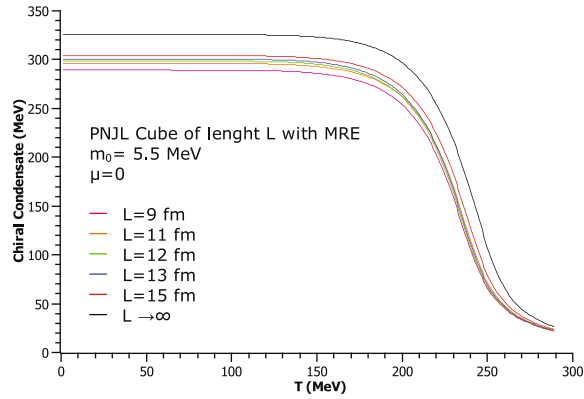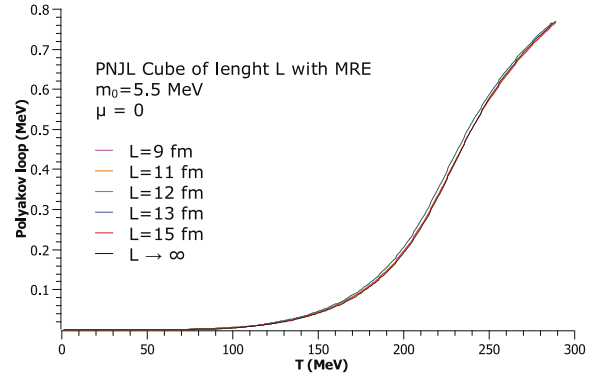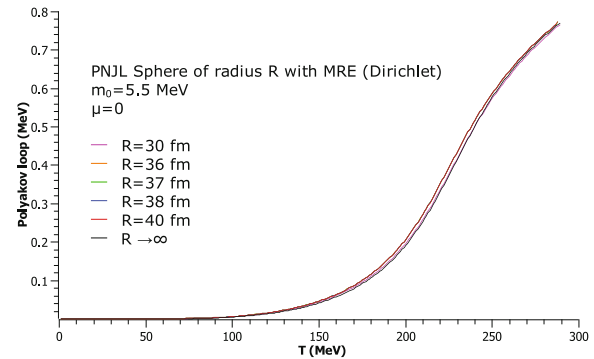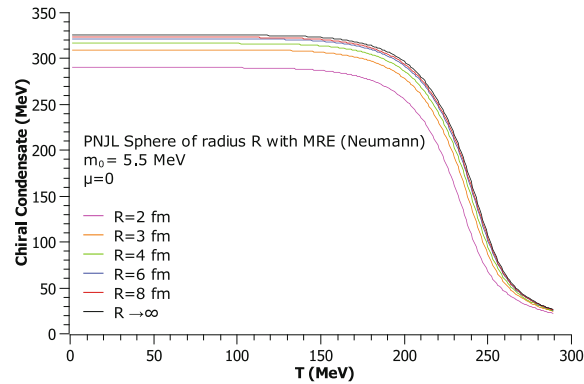

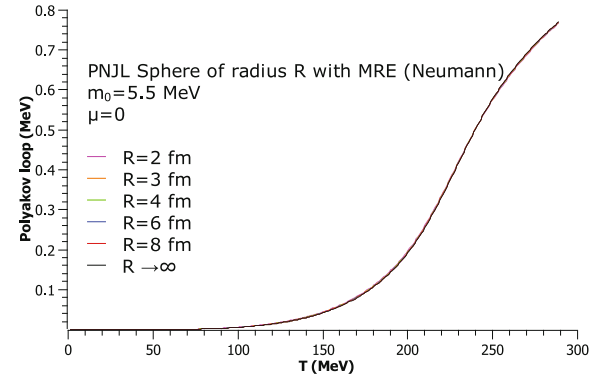**Figure 1:** Chiral condensate and Polyakov loop as functions of temperature for the PNJL model with the MRE approximation (polynomial potential) for different cases with $m_0 = 5.5$ MeV. (a) Chiral condensate for a cube. (b) Polykov loop for a cube. (c) Chiral condensate for a sphere with Dirichlet conditions. (d) Polyakov loop for a sphere with Dirichlet conditions. (e) Chiral condensate for a sphere with Neumann conditions. (f) Polyakov loop for a sphere with Neumann conditions.

Table 1: Constituent mass for m_0 = 5.5 MeV using the PNJL model in a finite volume, for different sizes and geometries

Constituent mass M	
	m_o = 5.5 MeV
L (fm)	M (MeV)
PNJL MRE cube	
15	303.94
13	300.55
12	298.42
11	295.90
9	289.11
PNJL MRE$_D$ sphere	
R (fm)	M (MeV)
40	300.21
38	298.86
37	298.12
36	297.35
30	291.61
PNJL MRE$_N$ sphere	
R (fm)	M (MeV)
8	323.22
6	321.46
4	316.49
3	309.61
2	290.12

conditions and $\Lambda_{\mathrm{IR}} = 1/(\sqrt{2}R)$ for the Neumann conditions [37,39].

4.2 Cubic volume

In this subsection, we extend the application of the MRE approximation to a cubic box shape. We obtain an expression for ρ_{MRE}, which can be applied to a cube, and it is simple to implement. We use this approximation for a cubic finite volume in the framework of chiral symmetry that includes deconfinement.

Eq. (23) shows that the density of states is composed of three terms. We extend the MRE approximation by observing the following changes to the expression for ρ_{MRE}: a cube with side L is defined for the surface term ρ_{surf} and a value of zero is assigned to the curvature factor f_C due to the fact that the surfaces of the cube are flat planes.

Since $f_C = 0$ for the curvature factor in Eq. (21), only volumetric and surface terms are developed. For the volumetric term, we observe that the integrand in thermodynamic potential is spherically symmetric, which means

that $d^3p = 4\pi p^2 dp$, which can be used to obtain the volumetric density of states:

$$\rho_{\mathrm{vol}} = \frac{1}{V}\frac{dN_v}{dp} = \frac{p^2}{2\pi^2}. \tag{32}$$

For the surface term, we proceed in an analog way to Eq. (32). The surface density of states is $dN_s = Ad^2\boldsymbol{p}/(2\pi)^2$, where $A = 6L^2$ is the area of the cube with side L; since $d^2\boldsymbol{p} = 2\pi p dp$, then the surface term of Eq. (21) is given by:

$$\left(\frac{dN_s}{dp}\right)f_S = \frac{Ap}{2\pi}\left(-\frac{1}{8\pi}\right) = -\frac{6L^2Lp}{16L\pi^2}. \tag{33}$$

Using Eqs (32) and (33), and with $\rho = \frac{1}{V}\frac{dN}{dp}$, the expression for the density of states is

$$\rho_{\mathrm{MRE}} = \frac{p^2}{2\pi^2}\left[1 - \frac{3}{4Lp}\right]. \tag{34}$$

In this case, the non-physically acceptable values are those in the interval between $p = 0$ and $p = 3/4L$, and consequently, the infrared cutoff is set to $\Lambda_{\mathrm{IR}} = 3/4L$.

5 Model parameters

The values of the regularization parameters that were used in this study are Λ = 651 MeV and G = 10.08 × 10⁻⁶ MeV⁻²; and for the quark mass m_o = 5.5 MeV, the mass and decay constant of pion are m_π = 139 MeV and f_π = 92.3 MeV, respectively; and the value for the quark condensate of $\langle\bar{u}u\rangle^{1/3}$ = 251 MeV. These values were reported by previous studies [29,41,42].

6 Results

6.1 Order parameters with finite volume for $\mu = 0$

By solving the gap equations in a self-consistent way, we can map the behavior of the order parameters: the chiral condensate and the Polyakov loop with respect to temperature, considering $\mu = 0$, and a polynomial potential.

The left-hand side of Figure 1(a, c, and e) shows the variation of the chiral condensate for different types of geometries where each line represents a definite volume. We start with a small volume sizes, which gradually varies
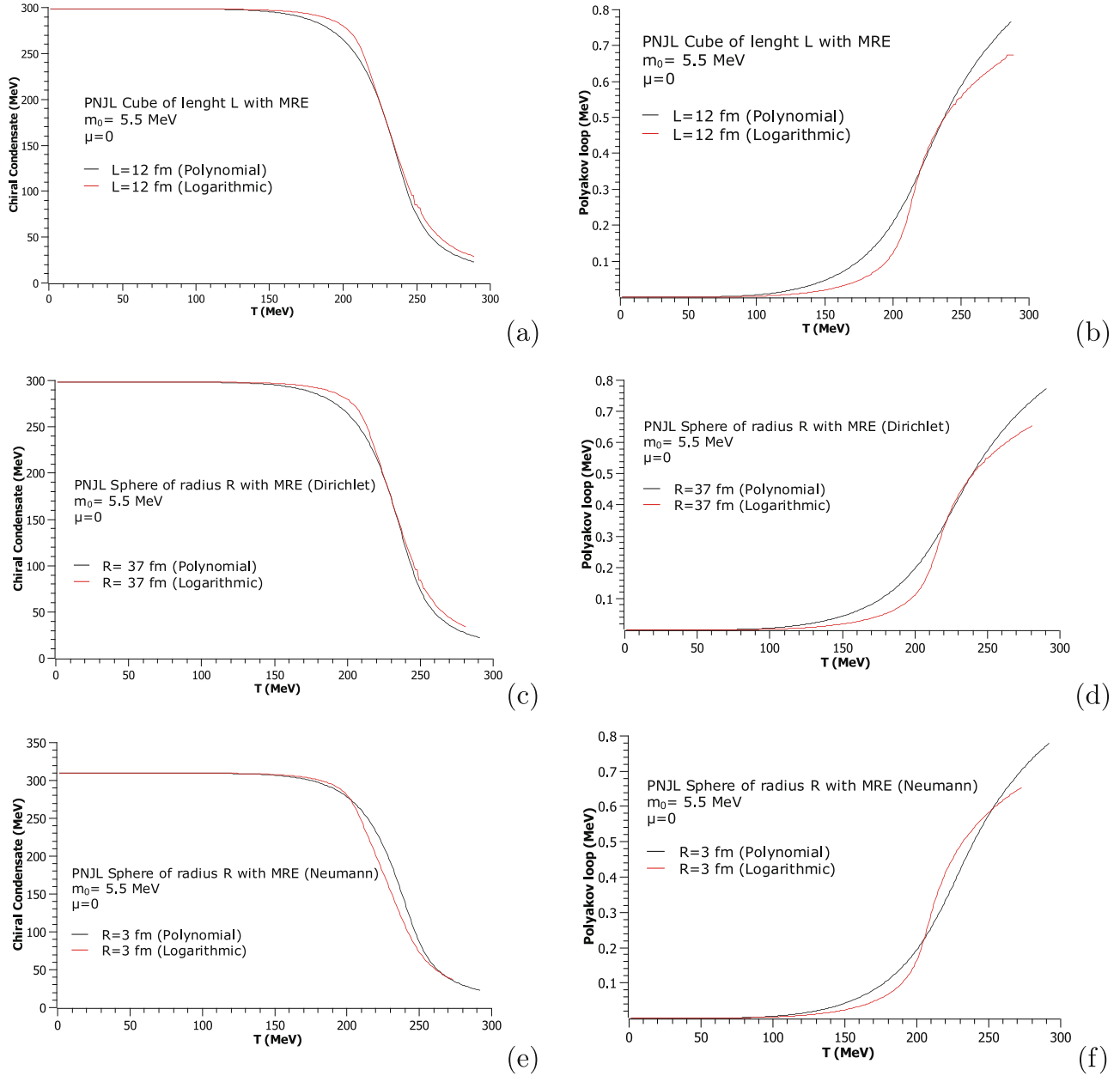
Figure 2: Chiral condensate and Polyakov loop as a function of temperature for the PNJL model with the MRE approximation for the polynomial and logarithmic potential with m_0 = 5.5 MeV. (a) Chiral condensate for a cube with L = 12 fm. (b) Polykov loop for a cube with L = 12 fm. (c) Chiral condensate for a sphere with Dirichlet conditions with R = 37 fm. (d) Polyakov loop for a sphere with Dirichlet conditions with R = 37 fm. (e) Chiral condensate for a sphere with Neumann conditions with R = 3 fm. (f) Polyakov loop for a sphere with Neumann conditions with R = 3 fm.

by increasing the radius or length of each geometry. We also compare these results when we have infinite volume (this occurs when the density of states is $\rho = \frac{p^2}{2\pi^2}$). As we make our system larger, we see a certain trend of the curve, a larger dynamically generated mass for low temperatures. Table 1 summarizes the chiral condensate for the different geometries and sizes.

The right panel (b, d, and f) shows the Polyakov loop making the same considerations of geometry and finite volume. Recall that in the PNJL model, the values different from zero imply deconfinement. On the other hand, we can see that the chiral symmetry restoration almost occurs simultaneously (for approximately the same temperature and chemical potential) with the confinement–deconfinement transition.
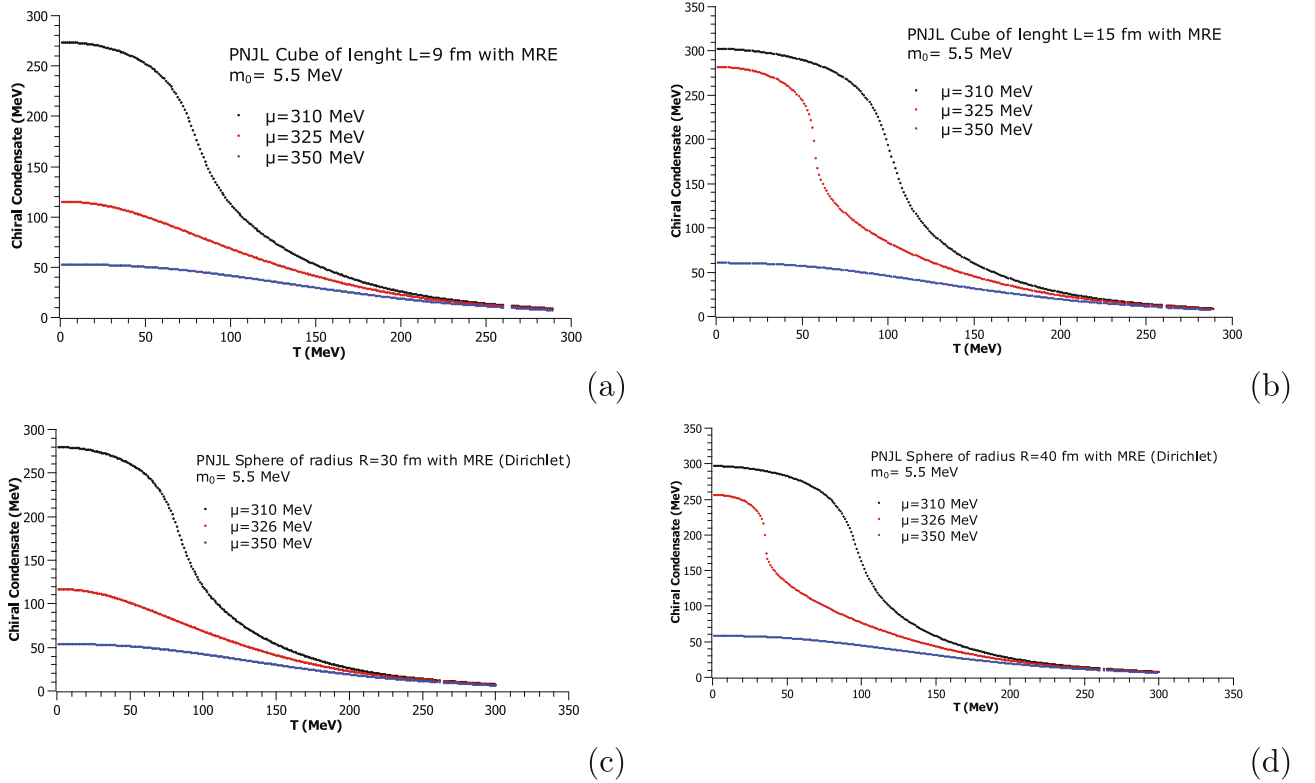
Figure 3: Variation of the condensate for different values of the chemical potential for a cube and sphere with the MRE appoximation (polynomial potential). We use three chemical potentials: μ = 310, 325 and 350 MeV for a cubic volumen and μ = 310, 326, 350 MeV for a spherical volume with the Dirichlet conditions. Variation of the condensate for the cube with (a) L = 9 fm and (b) L = 15 fm. Variation of the condensate for a sphere with (c) R = 30 fm and (d) R = 40 fm.

6.1.1 Polynomial vs logarithmic potential for $\mu = 0$

As we mentioned earlier, depending on the $\mathcal{U}(\varphi, \varphi^*; T)$ potential used in the model, the behavior of the chiral condensate and Polyakov loop will change. To determine this behavior, we modified the polynomial potential to a logarithmic one and performed the same procedure to see the changes in the graphs.

In the Figure 2 in (a) and (c) shows the curves for the chiral condensate at both potentials. By comparing them (for the cube and sphere with the Dirichlet conditions), we note that for a logarithmic potential, slightly higher temperatures are needed for the chiral condensate to decrease. On the other hand, for a sphere with the Neumann conditions (e), the behavior is completely the opposite, since lower temperatures are needed for the logarithmic potential.

In the Figure 2 in (b) and (d) we have the Polyakov loop represented and something similar happens. The behavior for the cube and sphere with the Dirichlet conditions is very similar; for a logarithmic potential, it needs higher temperatures for Φ parameter to grow. However, in the logarithmic potential, the Polyakov loop for the Neumann conditions seems to grow very fast for temperatures between $T \approx$ 200–250 MeV.

6.2 Order parameters with finite volume for $\mu \neq 0$

Variations of the order parameter as a function of temperature for several chemical potentials are shown in Figure 3.

In Figure 3, the plots in the left panel represent the behavior of the chiral condensate for different chemical potentials for the cubic and spherical geometry, respectively, considering a small volume L = 9 fm (a) and R = 30 fm (c). However, in the right panel, we now consider a larger volume for both geometries L = 15 fm (b) and R = 40 fm (d).

We observe that for small volumes, the condensate graph behaves smoothly and continuously. Unlike for larger volumes, where for a chemical potential of $\mu \approx$ 325 MeV, we could not ensure its continuity due to the visible gaps. There
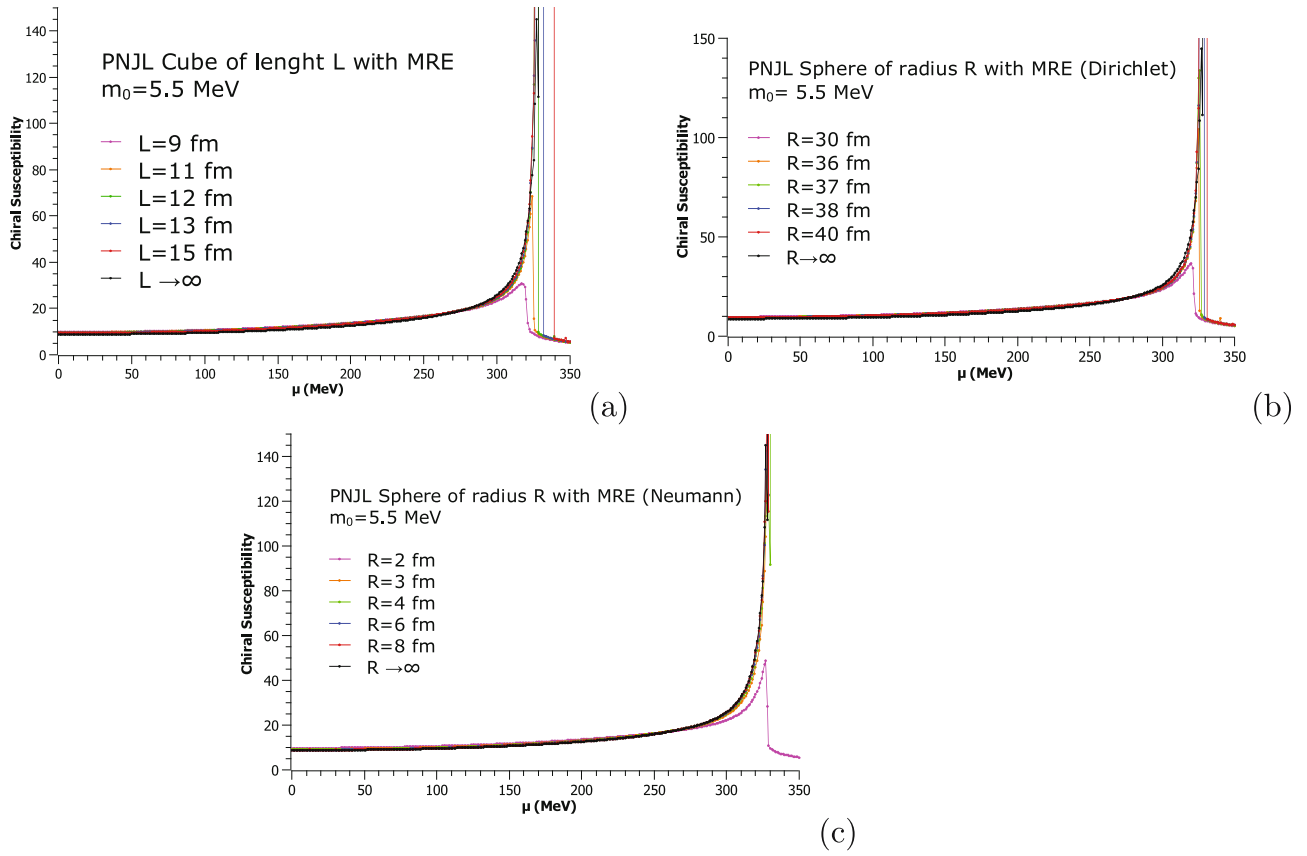
Figure 4: Maximal chiral susceptibility VS chemical potential for the PNJL model with the MRE approximation for: (a) cube, (b) sphere with Dirichlet conditions and (c) sphere with Neumann conditions.
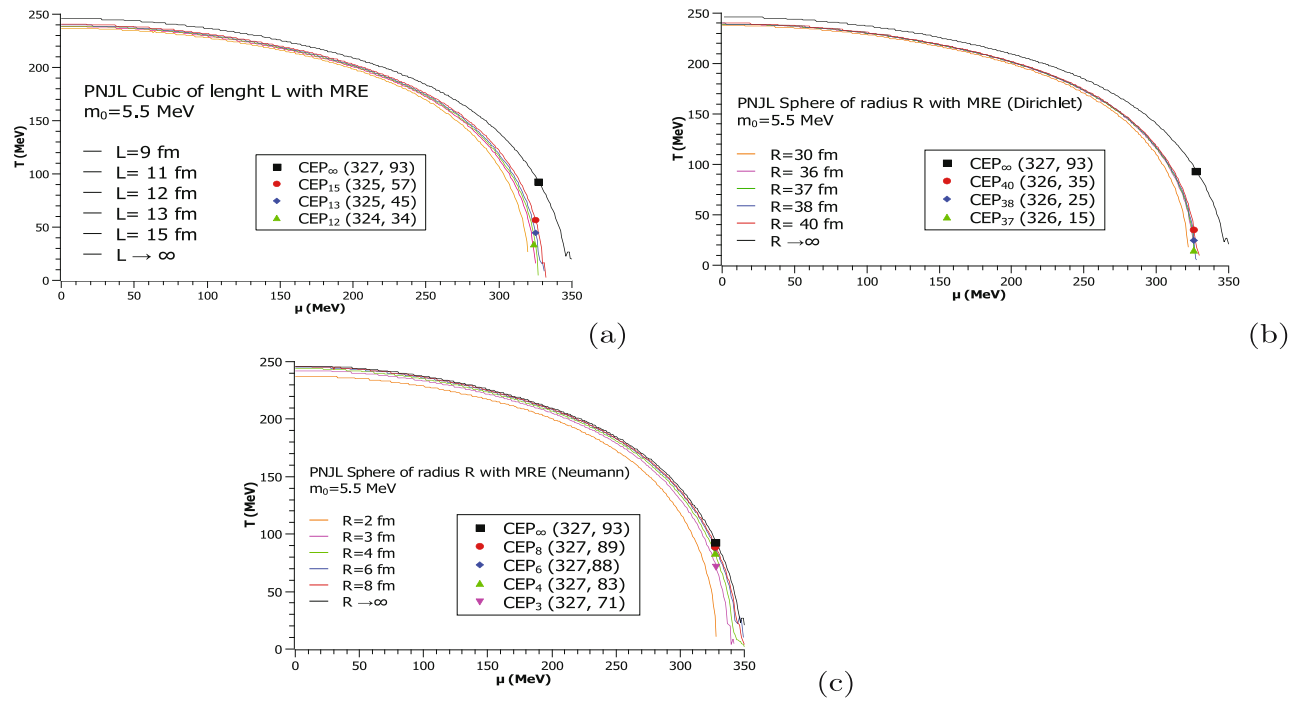

Figure 5: Phase diagram of the PNJL model in a finite volume with MRE appoximation for: (a) cube, (b) sphere with Dirichlet conditions and (c) sphere with Neumann conditions.

Table 2: CEP for the PNJL model in a finite volume using the MRE approximation with the traditional cutoff [42]

PNJL MRE$_D$ sphere

R (fm)	CEP (μ (MeV), T (MeV))
$R \gg 1$	**(329, 97)**
50	(326, 57)
40	(326, 35)
38	(326, 25)
<35	—

PNJL MRE cube

L (fm)	CEP (μ (MeV), T (MeV))
$L \gg 1$	**(329, 97)**
40	(326, 87)
15	(326, 58)
13	(325, 28)
<11	—

PNJL MRE$_N$ sphere

R (fm)	CEP (μ (MeV), T (MeV))
$R \gg 1$	**(329, 97)**
20	(327, 94)
10	(327, 93)
8	(327, 92)
6	(327, 90)
4	(327, 84)
3	(328, 72)
< 2	—

Table 3: Chiral temperature T_{ch} for $\mu = 0$ in the PNJL model in a finite volume, for different volume sizes and geometries for m_o = 5.5 MeV

PNJL MRE cube

Chiral temperature T_{ch}

L (fm)	m_o = 5.5 MeV T_{ch} (MeV)
15	241
13	240
12	239
11	239
9	237

PNJL MRE$_D$ sphere

Chiral temperature T_{ch}

R (fm)	m_o = 5.5 MeV T_{ch} (MeV)
40	300.21
38	298.86
37	298.13
36	297.35
30	291.61

PNJL MRE$_N$ sphere

Chiral temperature T_{ch}

R (fm)	m_o = 5.5 MeV T_{ch} (MeV)
8	246
6	245
4	244
3	242
2	237

is an abrupt drop in the plot at $T \approx 57$ MeV in the cube and $T \approx 35$ MeV in the sphere, which is a clear sign of a change in the type of phase transition that is associated with the existence of the CEP.

6.3 Susceptibilities

Susceptibility determines the rate of change of the thermodynamic potential with respect to a variation on the current quark mass [43,44]. Chiral susceptibility, which is the one we will concentrate on, determines the change of the constituent quark mass under a variation in the current quark mass. Chiral susceptibility is a probe to analyze the nature of the phase transition by identifying singularities in it.

We calculate the matrix of susceptibilities as:

$$\chi = \begin{pmatrix} \chi_{MM} & \chi_{M\Phi} & \chi_{M\Phi^*} \\ \chi_{\Phi M} & \chi_{\Phi\Phi} & \chi_{\Phi\Phi^*} \\ \chi_{\Phi^*M} & \chi_{\Phi^*\Phi} & \chi_{\Phi^*\Phi^*} \end{pmatrix}^{-1}, \tag{35}$$

where each component of the matrix is the second derivative of the thermodynamic potential with respect to the order parameters. We define χ_{MM} as the chiral susceptibility:

$$\chi_{MM} = \frac{1}{T\Lambda}\partial_{MM}\Omega, \quad \chi_{M\Phi} = \frac{1}{T\Lambda^2}\partial_{M\Phi}\Omega,$$

$$\chi_{\Phi\Phi} = \frac{1}{T\Lambda^3}\partial_{\Phi\Phi}\Omega, \quad \chi_{\Phi\Phi^*} = \frac{1}{T\Lambda^3}\partial_{\Phi\Phi^*}\Omega, \tag{36}$$

$$\chi_{\Phi^*\Phi^*} = \frac{1}{T\Lambda^3}\partial_{\Phi^*\Phi^*}\Omega, \quad \text{and} \quad \chi_{\Phi^*M} = \frac{1}{T\Lambda^2}\partial_{\Phi^*M}\Omega.$$

6.4 Chiral susceptibility

As mentioned earlier, finding singularities in the chiral susceptibility allows us to determine the nature of the phase
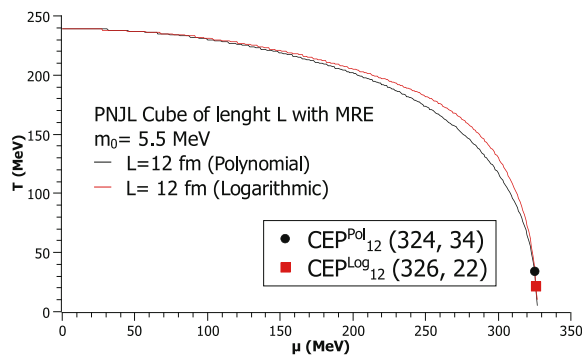
Table 4: CEP for the PNJL model in a finite volume using the MRE approximation for a polynomial and logarithmic potential

PNJL MRE cube

$\mathcal{U}$	L (fm)	CEP (μ [MeV], T [MeV])
Polynomial	12	(324, 34)
Logarithmic	12	(326, 22)

PNJL MRE_D sphere

$\mathcal{U}$	R (fm)	CEP (μ [MeV], T [MeV])
Polynomial	37	(326, 15)
Logarithmic	37	(325, 34)

PNJL MRE_N sphere

| $\mathcal{U}$	R (fm)	CEP (μ (MeV), T (MeV))
Polynomial	3	(327, 71)
Logarithmic	3	(327, 80)

transitions and it can help us in determining the existence of a CEP [45]. For example, by observing the behavior of the maximum chiral susceptibility (Figure 4), where we can vary the chemical potential and the size of the volume depending on each geometry, we can see an asymptotic trend as we increase the size of our system. The units of chiral susceptibility are dimensionless.

This behavior allows us to introduce certain criteria to determine the existence of the CEP, with which we can identify the size of the volume that allows each geometry to have a phase transition. Numerically, a very simple way to find the point where the nature of the phase transition changes, for example, from a crossover to first-order one, is by calculating the angle formed with respect to the horizontal axis by two consecutive points. We have chosen the criterion that when the slope exceeds the value ($\geq 89°$) is when we determine that our system presents a singularity. In this case, a change in the nature of the phase transition occurs, from a crossover to a first-order one at that point (μ, T). We will use the notation (μ[MeV], T [MeV]) to represent the sets of numbers, where μ denotes the chemical potential in units of MeV and T represents the temperature in MeV. Thus, a set such as (324, 24) corresponds to a value of μ of 324 MeV and a value of T of 34 MeV. This convention
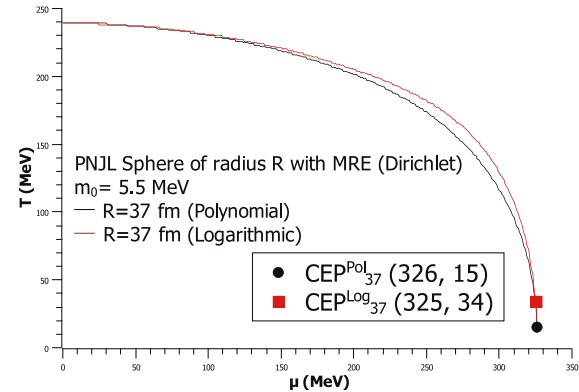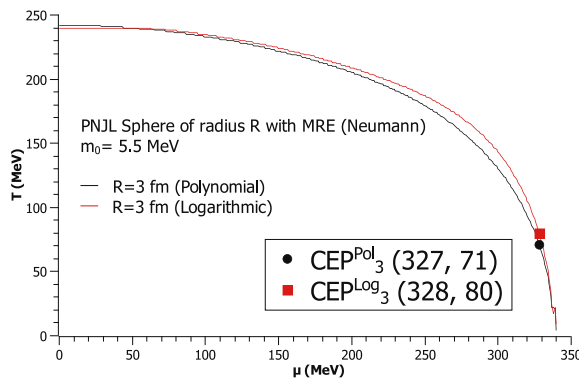
Figure 6: Phase diagram of the PNJL model in a finite volume with MRE approximation for: (a) cube with $L = 12$ fm for polynomial and logarithmic potential, (b) sphere with $R = 37$ fm for polynomial and logarithmic potential with Dirichlet conditions and (c) $R = 3$ fm for polynomial and logarithmic potential with Neumann conditions.

will be maintained throughout this article unless expressly stated otherwise.

7 Phase diagrams

To find the phase diagram, we will take the so-called local criterion, which takes the relative maximum value of the susceptibility at each iteration of the temperature and chemical potential. Thus, if the susceptibility has a vertical asymptote, we obtain a first-order phase transition. Using the criterion for locating the aforementioned CEP, we can represent the coordinate in the $T-\mu$ plane (Figure 5).

Analyzing the phase diagrams for each geometry, we can observe that depending on the size of the volume, there is a notorious change in the phase line. As we increase the size of the sphere radius or the side of the cube, the critical temperature increases.

Table 5: CEP for PNJL model in a finite volume using MRE approximation

PNJL MRE cube	
L (fm)	CEP (μ [MeV], T [MeV])
$L \gg 1$	(327, 93)
15	(325, 57)
13	(325, 45)
12	(324, 34)
<11	—

PNJL MRE$_D$ sphere	
R (fm)	CEP (μ [MeV], T [MeV])
$R \gg 1$	(327, 93)
40	(326, 35)
38	(326, 25)
37	(326, 15)
< 36	—

PNJL MRE$_N$	
R (fm)	CEP (μ (MeV), T (MeV))
$L \gg 1$	(327, 93)
8	(327, 89)
6	(327, 88)
4	(327, 83)
3	(327, 71)
<2	—

Left, cube of length L. Center, for a sphere of radius R with the Dirichlet conditions. Right, for a sphere with the Neumann conditions.

In addition, the occurrence of the CEP varies in each geometry. For a cube, the first phase transition occurs around $L = 12$ fm, where the CEP is located at (324, 34). For a spherical geometry where the conditions are of Dirichlet type, the first appearance of the CEP is at a radius of $R = 37$ fm, located at coordinate (326, 15). However, for the Neumann-type conditions, the first CEP is located for very small volumes as small as $R = 3$ fm, whose location is at (327, 71). For sizes smaller than those already mentioned in each geometry, no signs of a phase transition were found (with our criteria).

Table 2 shows the information for each point where the CEP was found for all geometries and different sizes of volume, and Table 3 shows the critical temperature.

7.1 Phase diagram with polynomial and logarithmic potential

We compare the phase diagrams for different geometries by choosing the volume size where we first locate the CEP. We observe that for the spherical geometry (Dirichlet and Neumann) with the polynomial potential, the CEP is at lower temperature compared to the logarithmic potential. In contrast, the opposite occurs for cubic geometry, as higher temperatures are needed to locate the CEP. These results are presented in Table 4 and Figure 6.

8 Discussion

The PNJL model in SU(2) is one of the most widely used effective models in QCD to describe the behavior of a system of particles interacting with the strong force. Three considerations were implemented under this model: finite volume effects using the MRE approximation, a soft cutoff regularization scheme, and two different Polyakov loop potentials (polynomial and logarithmic).

In addition, we have considered two different types of geometries that modify the density of states: cubic and spherical geometry (subject to the Dirichlet and Neumann boundary conditions). The current mass of the quarks was fixed at $m_0 = 5.5$ MeV. The soft cutoff regularization scheme was introduced so that our model can respect the Stefan–Boltzmann limit; by splitting the convergent integral where momenta are larger than the three-dimensional UV cutoff, fermionic interactions are no longer taken into account.

With these considerations, we focused on studying the behavior of the chiral condensate as well as the phase

diagrams, and by certain criteria, we obtained the coordinates of the CEP. It is interesting to note that using the soft cutoff regularization, this model appears to exhibit slightly enhanced accuracy, as evidenced by the shift of CEP values toward a slightly smaller volume. A more comprehensive visualization of these changes can be observed by comparing the results obtained in the study by Betancourt *et al.* [42], as presented in Table 2, with the findings in Table 5.

We have made significant findings regarding the CEP under various geometric configurations and boundary conditions. When using a soft cutoff regularization model in a cubic geometry, the CEP only manifests itself at a size of L = 12 fm, with coordinates located at (324, 34). In contrast, under the traditional cutoff, the CEP first appears at L = 13 fm, situated at (325, 28).

For a spherical geometry with the Dirichlet boundary conditions, the CEP emerges at a size of R = 37 fm, with coordinates at (326, 15), when using the soft cutoff. Conversely, with the traditional cutoff, the CEP becomes apparent at R = 38 fm, positioned at (326, 25).

Finally, in a spherical geometry with the Neumann boundary conditions, the CEP is found at R = 3 fm in both cases. However, it is worth noting that when using a soft cutoff, the CEP coordinates are (327, 71), whereas with the traditional cutoff, they are (328, 72).

Once we have located the size where the CEP first appears in each geometry, we can observe how this point changes depending now on the size. It was found that for the two types of geometries, the CEP always lies in $\mu \approx 326$ MeV. On the other hand, the temperatures increase as we expand our volume being the limit (327, 93), when we consider an infinite volume.

Finally, in the volume size where CEP first appeared in each geometry, the polynomial and logarithmic Polyakov loop potentials were compared. We note that depending on the potential, we choose the location of the CEP changes. We found that for a spherical geometry (the Dirichlet and Neumann conditions), higher temperatures are needed to locate the CEP with a logarithmic potential. On the other hand, for a cubic geometry, the opposite occurs; using a logarithmic potential, the presence of the CEP requires lower temperatures than in a polynomial potential.

Author contributions: All authors have accepted responsibility for the entire content of this manuscript and approved its submission.

References

[1]   Oaknin DH, Zhitnitsky A. Baryon asymmetry, dark matter, and quantum chromodynamics. Phys Rev D. 2005;71:023519.

[2]   Kurkela A, Fraga ES, Schaffner-Bielich J, Vuorinen A. Constraining neutron star matter with quantum chromodynamics. Astrophys J. 2014;789(2):127.

[3]   Bratovic N, Hatsuda T, Weise W. Role of vector interaction and axial anomaly in the PNJL modeling of the QCD phase diagram. Phys Lett B. 2013;719(1–3):131–5.

[4]   Lu Y, Cui Z-F, Pan Z, Chang C-H, Zong H-S. QCD phase diagram with a chiral chemical potential. Phys Rev D. 2016;93(7):074037.

[5]   Bazavov A, Bhattacharya T, Cheng M, DeTar C, Ding H-T, Gottlieb S, et al. Chiral and deconfinement aspects of the QCD transition. Phys Rev. 2012;85:054503.

[6]   McLerran L, Redlich K, Sasaki C. Quarkyonic matter and chiral symmetry breaking. Nucl Phys A. 2009;824(1–4):86–100.

[7]   Nakano TZ, Miura K, Ohnishi A. Chiral and deconfinement transitions in strong coupling lattice QCD with finite coupling and Polyakov loop effects. Phys Rev D. 2011;83:016014.

[8]   Digal S, Laermann E, Satz H. Deconfinement through chiral symmetry restoration in two-flavour QCD. Eur Phys J C Part Fields. 2001;18(3):583–6.

[9]   Costa P, de Sousa CA, Ruivo MC, Hansen H. The QCD critical end point in the PNJL model. EPL. 2009;86(3):31001.

[10] Costa P, de Sousa CA, Ruivo MC, Kalinovsky YL. The QCD critical end point in the SU(3) Nambu-Jona-Lasinio model. Phys Lett B. 2007;647(5–6):431–5.

[11] Gavai RV, Gupta S. The critical end point in QCD. Nucl Phys A. 2007;785(1–2):18–23.

[12] Bernhardt J, Fischer CS, Isserstedt P, Schaefer B-J. Critical endpoint of QCD in a finite volume. Phys Rev D. 2021;104(7):074035.

[13] Blume C. Search for the critical point and the onset of deconfinement. Open Phys. 2012;10(6):1245–53.

[14] Ayala A, Bashir A, Cobos-Martínez JJ, Hernández-Ortiz S, Raya A. The effective QCD phase diagram and the critical end point. Nucl Phys B. 2015;897:77–86.

[15] Cui Z-F, Hou F-Y, Shi Y-M, Wang Y-L, Zong H-S. Progress in vacuum susceptibilities and their applications to the chiral phase transition of QCD. Ann Phys (N Y). 2015;358:172–205.

[16] Redlich K. Probing the QCD chiral cross-over transition in heavy ion collisions. Open Phys. 2012;10(6):1254–7.

[17] Yuanfang W, Lizhu C, Xue P, Ming S, Chen X. Finite-size behaviour of a critical related observable. Open Phys. 2012;10(6):1341–4.

[18] Xu F, Huang M. The chiral and deconfinement phase transitions. Open Phys. 2012;10(6):1357–60.

[19] Mukherjee S, Mustafa MG, Ray R. Thermodynamics of the Polyakov-Nambu-Jona-Lasinio model with nonzero baryon and isospin chemical potentials. Phys Rev D. 2007;75:094015.

[20] Ghosh SK, Mukherjee TK, Mustafa MG, Ray R. Susceptibilities and speed of sound from the Polyakov-Nambu-Jona-Lasinio model. Phys Rev D. 2006;73:114007.

[21] Abuki H, Anglani R, Gatto R, Nardulli G, Ruggieri M. Chiral crossover, deconfinement, and quarkyonic matter within a Nambu-Jona-Lasinio model with the Polyakov loop. Phys Rev D. 2008;78:034034.

[22] Valbuena-Ordóñez E, Mata-Carrizal NB, Garza-Aguirre AJ, Morones-Ibarra JR. Influence of the effective potential on the crossover width in the two flavor Polyakov-Nambu-Jona-Lasinio model. Adv High Energy Phys. 2020;2020:1–14.

[23] Mukherjee TK, Chen H, Huang M. Chiral condensate and dressed Polyakov loop in the Nambu-Jona-Lasinio model. Phys Rev D. 2010;82:034015.

[24] Cui Z-F, Du Y-L, Zong H-S. The two-flavor NJL model with two-cutoff proper time regularization. Int J Mod Phys Conf Ser. 2014;29:1460232.

[25] Blanquier E. Standard particles in the SU(3) Nambu-Jona-Lasinio model and the Polyakov-NJL model. J Phys G Nucl Part Phys. 2011;38(10):105003.

[26] Fukushima K. Chiral effective model with the Polyakov loop. Phys Lett B. 2004;591(3–4):277–84.

[27] Fukushima K, Ruggieri M, Gatto R. Chiral magnetic effect in the Polyakov-Nambu-Jona-Lasinio model. Phys Rev D. 2010;81:114031.

[28] Fukushima K. Phase diagrams in the three-flavor Nambu-Jona-Lasinio model with the Polyakov loop. Phys Rev D. 2008;77:114028.

[29] Ratti C, Thaler MA, Weise W. Phases of QCD: Lattice thermodynamics and a field theoretical model. Phys Rev D. 2006;73:014019.

[30] Roessner S, Ratti C, Weise W. Polyakov loop, diquarks, and the two-flavor phase diagram. Phys Rev D. 2007;75:034007.

[31] Avancini SS, Farias RLS, Pinto MB, Restrepo TE, Tavares WR. Regularizing thermo and magnetic contributions within nonrenormalizable theories. Phys Rev D. 2021;103(5):056009.

[32] Shao GY, Di Toro M, Greco V, Colonna M, Plumari S, Liu B, et al. Phase diagrams in the hadron-Polyakov-Nambu-Jona-Lasinio model. Phys Rev D. 2011;84:034028.

[33] Kohyama H, Kimura D, Inagaki T. Regularization dependence on phase diagram in Nambu-Jona-Lasinio model. Nucl Phys B. 2015;896:682–715.

[34] Morones-Ibarra JR, Mata-Carrizal NB, Valbuena-Ordóñez E, Garza-Aguirre AJ. Dependence of the crossover zone on the regularization method in the two-flavor Nambu-Jona-Lasinio model. Open Phys. 2020;18(1):089–103.

[35] Meissner T, Arriola ER, Goeke K. Regularization scheme dependence of vacuum observables in the Nambu-Jona-Lasinio model. Z Physik A - Atomic Nuclei. 1990;336(1):91–6.

[36] Kalinovsky YL, Toneev VD, Friesen AV. Phase diagram of baryon matter in the SU(2) Nambu – Jona-Lasinio model with a Polyakov loop. Phys-Usp. 2016;59(4):367–82.

[37] Kiriyama O, Kodama T, Koide T. Finite-size effects on the QCD phase diagram. arXiv [hep-ph]. 2006.

[38] Madsen J. Shell model versus liquid drop model for strangelets. Phys Rev D Particles Fields. 1994:50(5):3328–31.

[39] Kiriyama O. Color-superconducting strangelets in the Nambu-Jona-Lasinio model. Phys Rev D. 2005;72:054009.

[40] Kiriyama O, Hosaka A. Chiral phase properties of finite size quark droplets in the Nambu-Jona-Lasinio model. Phys Rev D. 2003;67:085010.

[41] Klevansky SP. The Nambu-Jona-Lasinio model of quantum chromodynamics. Rev Modern Phys. 1992;64(3):649–708.

[42] Betancourt FJ, Saucedo JR, Flores-Ocampo F, Flores-Baez FV, Paz A, Morones-Ibarra JR. QCD phase diagram in a finite volume in the PNJL model. Open Phys. 2022;20(1):377–89.

[43] Morones-Ibarra JR, Enriquez-Perez-Gavilan A, Rodriguez AIH, Flores-Baez FV, Mata-Carrizalez NB, Ordoñez EV. Chiral symmetry restoration and the critical end point in QCD. Open Phys. 2017;15(1):1039–44.

[44] Sasaki C, Friman B, Redlich K. Susceptibilities and the phase structure of a chiral model with Polyakov loops. Phys Rev D. 2007;75:074013.

[45] Rößner S, Hell T, Ratti C, Weise W. The chiral and deconfinement crossover transitions: PNJL model beyond mean field. Nucl Phys A. 2008;814(1–4):118–43.